



Quantum Behavior of Spin-Orbit Inelastic Scattering of C-Atoms by D₂ at Low Energy

Astrid Bergeat^{1*}, Sébastien B. Morales¹, Christian Naulin¹, Jacek Kłos² and François Lique³

¹ Univ. Bordeaux, CNRS, ISM, UMR 5255, Talence, France, ² Department of Chemistry and Biochemistry, University of Maryland, College Park, MD, United States, ³ LOMC - UMR 6294, CNRS-Université du Havre, Le Havre, France

Fine-structure populations and collision-induced energy transfer in atoms are of interest for many fields, from combustion to astrophysics. In particular, neutral carbon atoms are known to play a role in interstellar media, either as probes of physical conditions (ground state ³P_j spin-orbit populations), or as cooling agent (collisional excitation followed by radiative decay). This work aims at investigating the spin-orbit excitation of atomic carbon in its ground electronic state due to collisions with molecular deuterium, an isotopic variant of H₂, the most abundant molecule in the interstellar medium. Spin-orbit excitations of C(³P_j) by H₂ or D₂ are governed by non-adiabatic and spin-orbit couplings, which make the theoretical treatment challenging, since the Born-Oppenheimer approximation no longer holds. Inelastic collisional cross-sections were determined for the C(³P₀) + D₂ → C(³P_j) + D₂ (with *j* = 1 and 2) excitation process. Experimental data were acquired in a crossed beam experiment at low collision energies, down to the excitation thresholds (at 16.42 and 43.41 cm⁻¹, respectively). C-atoms were produced mainly in their ground spin-orbit state, ³P₀, by dissociation of CO in a dielectric discharge through an Even-Lavie pulsed valve. The C-atom beam was crossed with a D₂ beam from a second valve. The state-to-state cross-sections were derived from the C(³P_j) (*j* = 1 or 2) signal measured as a function of the beam crossing angle, i.e., as a function of the collision energy. The results show different quantum behaviors for excitation to C(³P₁) or C(³P₂) when C(³P₀) collides with *ortho*-D₂ or *normal*-D₂. These experimental results are analyzed and discussed in the light of highly accurate quantum calculations. A good agreement between experimental and theoretical results is found. The present data are compared with those obtained for the C-He and C-H₂ collisional systems to get new insights into the dynamics of collision induced spin-orbit excitation/relaxation of atomic carbon.

Keywords: chemical physics, dynamics of molecular collisions, inelastic collisions, astrochemistry, crossed-molecular beam, theoretical calculations, spin-orbit excitation

INTRODUCTION

Processes controlling internal state population distributions of atomic or molecular species are of interest in many fields. This is especially the case for astrophysics. In particular, information concerning the physical conditions prevailing in interstellar media can only be retrieved from spectra yielding the internal states relative populations of the observed species, which result from

OPEN ACCESS

Edited by:

Antonio Aguilar,
University of Barcelona, Spain

Reviewed by:

Robert Forrey,
Penn State Berks, United States
Stefan Willitsch,
Universität Basel, Switzerland

*Correspondence:

Astrid Bergeat
astrid.bergeat@u-bordeaux.fr

Specialty section:

This article was submitted to
Physical Chemistry and Chemical
Physics,
a section of the journal
Frontiers in Chemistry

Received: 02 January 2019

Accepted: 04 March 2019

Published: 28 March 2019

Citation:

Bergeat A, Morales SB, Naulin C,
Kłos J and Lique F (2019) Quantum
Behavior of Spin-Orbit Inelastic
Scattering of C-Atoms by D₂ at Low
Energy. *Front. Chem.* 7:164.
doi: 10.3389/fchem.2019.00164

the equilibrium between collisional and radiative processes. For that purpose, neutral carbon atoms are of particular interest, since they are known to play a role in interstellar media, either as probes of physical conditions (ground state ³P_j spin-orbit populations), or as a cooling agent (collisional excitation followed by a radiative decay). Indeed, C atoms are very abundant in many interstellar regions ranging from dense molecular clouds to planetary nebulae (Zmuidzinas et al., 1988; Bensby and Feltzing, 2006; Herbst and Yates, 2013). Hence, modeling the fine-structure population of C atoms is of major interest for astrochemical models. Such models rely on both collisional and radiative data. Collisional cross-sections and rate coefficients implying the C atoms and the dominant collisional partners in the interstellar medium (H₂, He, H) have then to be determined at low temperatures. However, when molecular collisions (reactive or inelastic) occur at low energy/temperature, in the *near cold* regime (1–50 K), resonances are predicted by theory for many systems. Such resonances have been clearly observed in the collision energy dependent integral cross-sections (ICS) for spin-orbit excitation of C(³P₀) by collisions with He (Bergeat et al., 2018) and H₂ (Kłos et al., 2018). These processes are governed by non-adiabatic and spin-orbit couplings, which makes the theoretical treatment challenging since the Born-Oppenheimer (Born and Oppenheimer, 1927) approximation no longer holds. The challenge was successfully overcome for the C(³P)+He two-atomic system (Bergeat et al., 2018): the excellent agreement between experimental results and theory allowed a detailed description of resonance features by theory to be obtained. The situation was quite more complex for the C(³P)+H₂ three-atomic system (Kłos et al., 2018), where multiple diabatic potential energy surfaces (PESs) along with spin-orbit and non-adiabatic couplings are necessary to describe its dynamics. A good agreement was also found, not sufficient however to allow for a clear assignment of resonances involving too great of a number of partial waves. Moreover, at higher collision energies, an intersystem crossing may occur with the PESs emerging from the C(¹D)+H₂ insertion reaction. In the energy regions close to the intersystem crossing, one can expect, that the use of only triplet PESs will be too approximate to describe the collisional excitation of the C atom, which was not investigated in the study of C+H₂ collisions (Kłos et al., 2018). Moreover, most recently, Shen et al. (2017) elucidated importance of the stationary points, in particular the so-called van der Waals saddles in the entrance channel region of the C(¹D)-H₂ reaction. Therefore, it is also of interest to confirm the characterization of the entrance channel in the C(³P)-H₂ system. Our experiments will allow to test the C(³P)-H₂ PESs in the lower region of collision energies.

In order to get a clearer insight into the latter system, new experiments and calculations have been performed on the isotopolog system so that the C(³P₀) + D₂ → C(³P_j) + D₂ (with *j* = 1 and 2) collisional process have been studied. Measurements of state-to-state cross-sections as a function of the collision energy for C(³P)-D₂ scattering have been achieved, using the same apparatus as the one described in our previous studies on C(³P)-He (H₂) inelastic collisions. Quantum dynamical calculations were performed with the same

TABLE 1 | Characteristics of the molecular beams used in the determination of the integral cross-sections.

Beam	Gas mixture	<i>T</i> ^a (K)	<i>v</i> ^b (ms ⁻¹)	δ <i>v</i> _{HWE} ^b (ms ⁻¹)	τ ₀ ^c (μs)	δ <i>α</i> ^d (°)
#1 C(³ P)	CO:0.3%/Ne	300	815 ± 11	13.5	8.6	1.1
#2 <i>o</i> -D ₂ or <i>n</i> -D ₂	Neat	100 (117)	1180 ± 19	53	9.9	1.69
#3 <i>o</i> -D ₂	Neat	45 (68)	855 ± 20	36.9	11	1.69
#3 <i>n</i> -D ₂	Neat	45 (68)	845 ± 12	36.9	11	1.69
#4 <i>o</i> -D ₂	Neat	10 (47)	694 ± 10	38	12.9	1.65

^aTemperature set point of the cold head. The effective temperature of the pulsed valve is limited by losses due to thermal radiation. The effective nozzle temperatures deduced from the He beam velocity are given in parentheses.

^bBeam velocity peak values and spreads were deduced from temporal profiles recorded at the crossing point by REMPI detection, and at *d* = 393.3 mm downstream, with a fast-ionization gauge (FIG) inserted perpendicular to the molecular beam.

^cPulse duration at the crossing point (hwe) deduced from the REMPI signals.

^dAngular divergence (HWE).

PESs as for C(³P)-H₂ system and differing by the reactant reduced mass and rotational constant of D₂: it thus provides a further test of these potential energy surfaces that are mandatory to accurately describe and understand the dynamics of the title system.

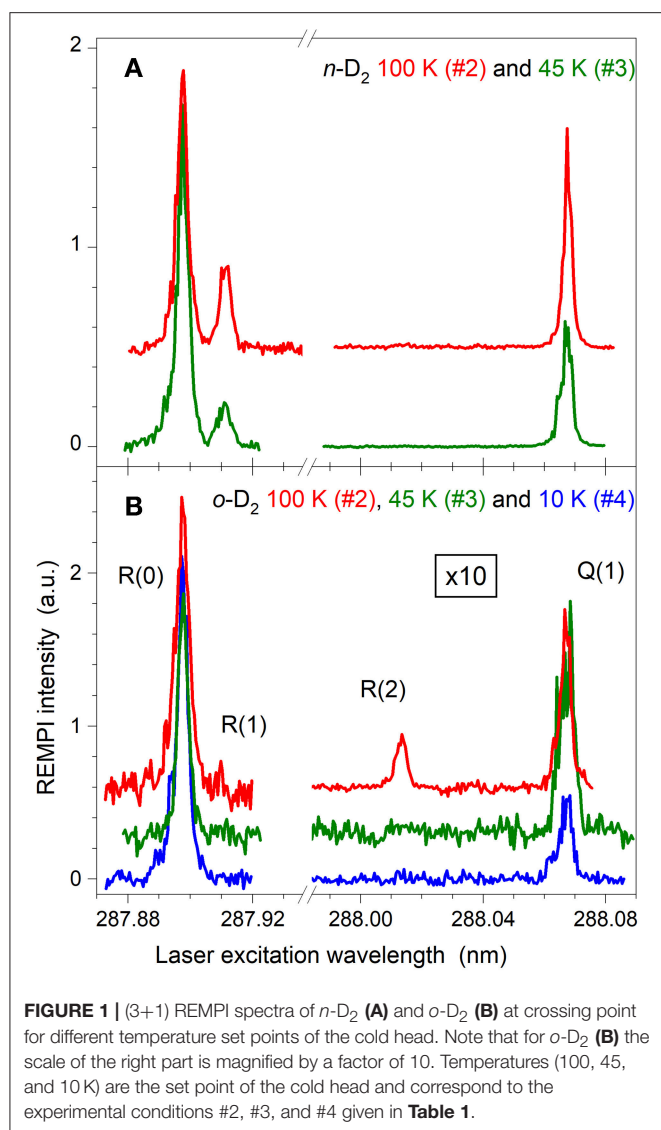
METHODS

Experiment

Integral cross-sections were measured using a crossed beam apparatus, with variable crossing angle. The C and D₂ beams with low velocities and high velocity resolution (see **Table 1**) were obtained using two cryogenically cooled Even-Lavie pulsed valves (Pentlehner et al., 2009) and collided at a beam intersection angle which could be continuously varied from 90° to 12.5° (Chefdeville et al., 2012). C-atoms were produced by dissociation of CO diluted in neon in a dielectric barrier discharge incorporated in the faceplate of the valve (Even, 2015). *ortho*-D₂ (hereafter *o*-D₂) was produced after spin-conversion in a cryogenic cell by liquefaction of *normal*-D₂ (hereafter *n*-D₂) on NiSO₄ catalyst at low temperature (<20 K), every 45 min. The *n*-D₂ and *o*-D₂ beam velocities were changed by adjusting the temperature of the valve cold head (see **Table 1** for the different experimental conditions).

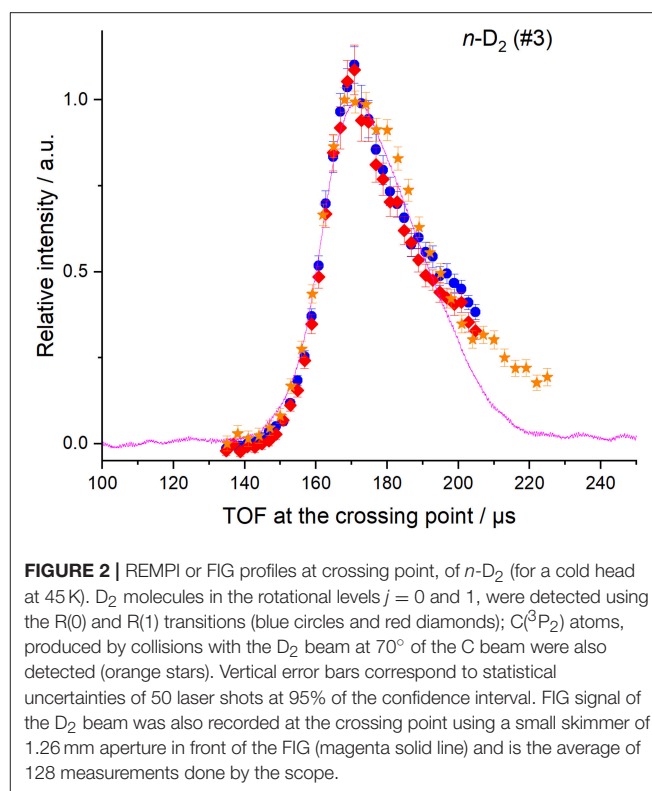
The collision energy, *E_T*, in our crossed beam machine was varied by changing the angle between the two supersonic beams from *χ* = 90° to 20 or 13°: $E_T = \frac{1}{2}\mu \left\{ v_C^2 + v_{D_2}^2 - 2v_C v_{D_2} \cos\chi \right\}$.

The carbon atoms were probed in their various spin-orbit states via (2+1) resonance-enhanced multiphoton ionization (REMPI) technique, using 2-photon 2p² ³P_j → 2p3p ³P_j transitions (excitation laser tuned at 280.3 nm) at 140.149 nm, 140.157 nm and 140.170 nm for the C(³P₀), C(³P₁) and C(³P₂), respectively (Geppert et al., 2003). A third photon ionized the carbon atoms and C⁺ is detected by a time-of-flight (TOF) mass spectrometer. Populations of *ca* 90–96% for C(³P₀), 4–10% for C(³P₁), and < 1% for C(³P₂) were deduced from the intensities of these transitions, consistently with previous

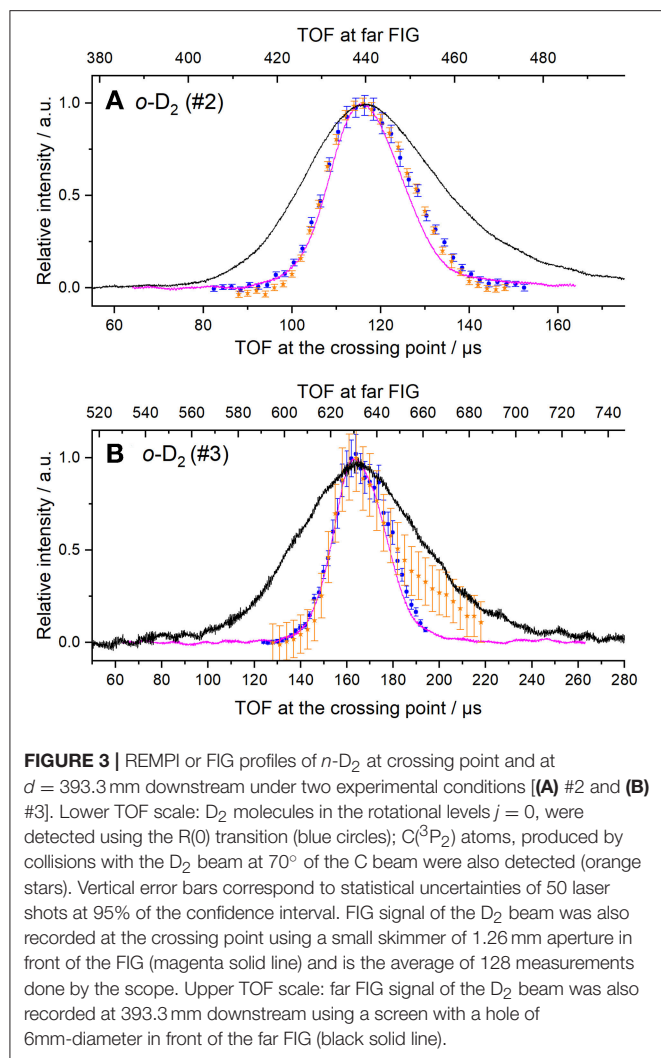


studies (Bergeat et al., 2018; Klos et al., 2018). The laser beam was perpendicular to the crossing beams plane, hence avoiding any Doppler shift while scanning the crossing angle, χ , for the ICS measurements. Spectra obtained by 3+1 REMPI on the transitions $C^1\Pi_u(v' = 3, j') \leftarrow X^1\Sigma_g^+(v'' = 0, j'')$ were employed to detect individual D₂ rotational levels (see **Figure 1**). Only the lowest rotational level of each nuclear spin modification, i.e., $j_{D_2} = 0$ and 1 for *o*-D₂ and *p*-D₂, respectively, was found to be populated in the supersonic beams. The only exception was for *o*-D₂, 100 K: a small signal can be seen for the R(2) transition. The *ortho* converted-D₂ was found to contain <6% *para*-D₂. These values were found to change inappreciably over the D₂ velocities (or the temperature of the valve) and over 1.5 h.

The beam velocities and spreads (**Table 1**) were deduced from temporal profiles recorded at the crossing point by REMPI detection or with a fast ionization gauge (FIG) inserted perpendicular to the molecular beam, and at $d = 393.3$ mm downstream, with a second FIG. D₂ can be detected with the

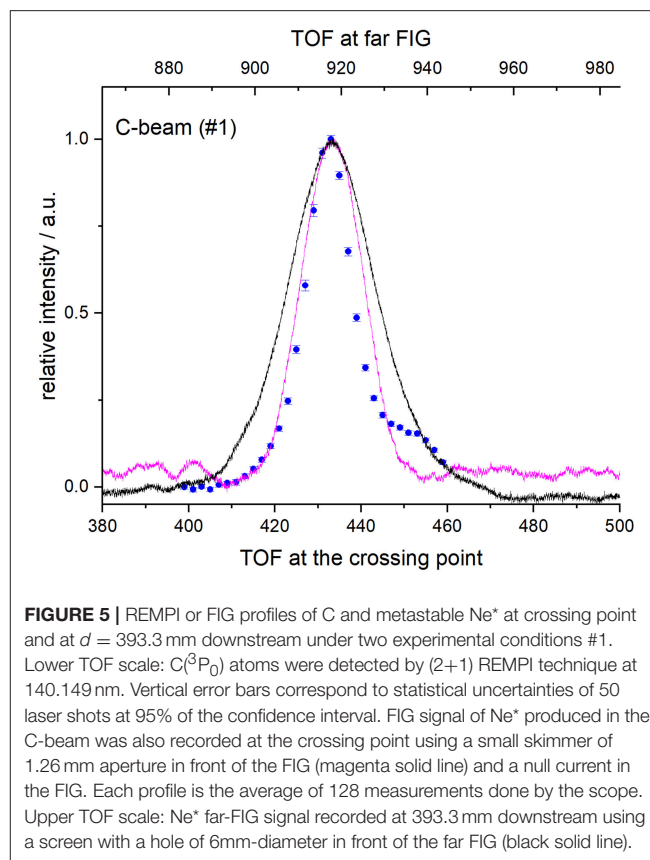
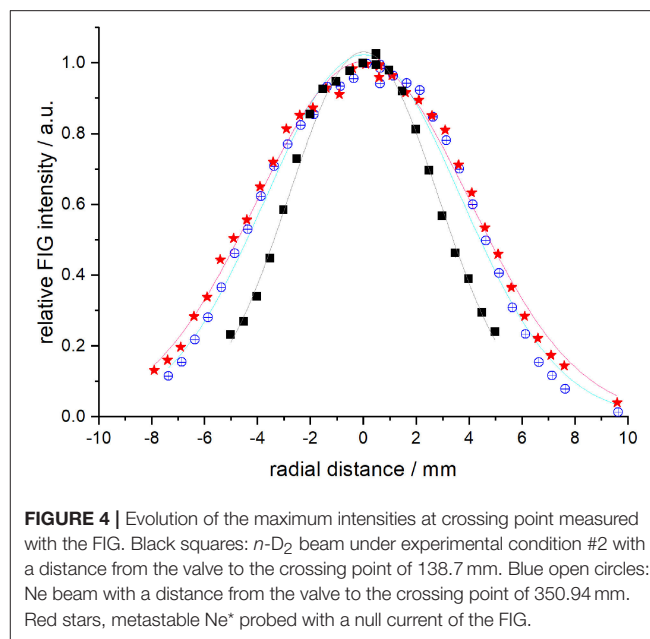


FIG, and by REMPI at the crossing point but not during the ICS measurements: it was then detected indirectly via the excited carbon C(³P_{1 or 2}) produced by collisions of C atoms with D₂. In the latter case, the trigger delay of the D₂ beam for the ICS measurements was adjusted to obtain a maximum REMPI signal of carbon atoms in the (³P₁) or (³P₂) states. Typical REMPI profiles obtained for D₂ produced in the experimental condition #3 where the cold head temperature was set at 45 K (**Table 1**) are given in **Figure 2**. To confirm the beam profiles obtained indirectly during the ICS measurements, two other experiments were also performed independently with the REMPI technique directly on D₂ molecules (see **Figure 1**) or with a FIG inserted perpendicular to the molecular beam. Typical results of time-of-flight (TOF) profiles are given **Figure 2** for *n*-D₂ beam in the experimental conditions #3. All the profiles of D₂ ($j_{D_2} = 0$ and 1) may be superimposed: only the intensities differ due to the population distribution, which means that all the rotational states are generated during the expansion and uniformly spread into the beam of *n*-D₂. Once the profile at the crossing point achieved, the D₂ beam arrival time, measured with the FIG at $d = 393.3$ mm downstream, yielded the D₂ velocity. All profiles were fitted to Gaussian functions, with peak positions t_0 and t_1 and half-width at 1/e (HWE), yielding the peak velocities $v = d / (t_1 - t_0)$, and the velocity spreads δv_{HWE} from the pulse broadening (Naulin and Bergeat, 2018). The response time of the FIG was previously determined to be ~ 3 μ s [see Supplementary Materials of Chevdeville et al. (2013)], and t_1 values are thus accordingly corrected. With this method, the velocities of the D₂ beam were checked, before, during and after the ICS measurements



of each day to ensure the absence of any drift. Typical results for o -D₂ generated under the conditions #2 and #4 are given in **Figure 3**. To determine the angular spread of the beam, the FIG at the crossing point, mounted on a translation stage, was moved perpendicularly to the beam axis to enable measurements at various positions. A depth gauge allows the exact re-positioning of the FIG. It should be noted that the TOF profiles don't change with the position of the FIG, which means that the transverse velocity is negligible compared to the beam velocity. The area of the TOF profiles or the maximum intensity varies with the position of the FIG: the angular spreads given in **Table 1** were determined by fitting the curves with Gaussian functions (see **Figure 4**).

Carbon atoms can only be detected by REMPI at the crossing point, but not with the FIG, contrarily to metastable Ne* atoms also generated within the discharge. They give a signal due to surface ionization with the FIG operated with a null filament current. Since C(³P) and Ne* profiles obtained by REMPI at the crossing point are very similar, it was assumed that their velocities were likely to be identical.



Again, beam profiles could also be measured at the crossing point when replacing the mass spectrometer by a FIG. The two profiles obtained for metastable Ne* are identical (see **Figure 5**). As for D₂, Ne* velocity values and spreads could

be determined from profiles at the crossing point and at $d = 393.3$ mm downstream.

ICSs were obtained from the averaged REMPI signal intensities I_{REMPI} and the relative velocity v_r of the C and D₂ beams as $I_{\text{REMPI}}/(v_r \langle \Delta t \rangle)$, where $\langle \Delta t \rangle$ is the mean interaction time between the two beam pulses which takes full account of the density-to-flux transformation under our working conditions (Naulin and Costes, 2014), and assuming a forward angular distribution of scattered C-atoms as for the C-H₂ system (Kłos et al., 2018). To monitor the efficiency of the discharge, the Ne* signal from the FIG 393.3 mm downstream the crossing point was used. Moreover, the UV laser was detected by a photodiode at the entrance of the main chamber. Data points acquired with poor discharge conditions and laser power lower than 80% of the average over the whole scan were not discarded. Since the densities of the two beams were not quantitatively determined, we could not extract absolute cross-sections. Relative experimental cross-sections for C(³P₀) + *o*-, *n*-D₂ → C(³P_{*j=1,2*}) + *o*-, *n*-D₂ inelastic collisions were obtained by accumulating at each angle signals from several thousand beam pulses. They were normalized by the sum of the experimental cross-sections in the energy ranges 22–114 cm⁻¹ for C(³P₀) → C(³P₁) transition, and 26–165 cm⁻¹ for C(³P₀) → C(³P₂) transition. All the plotted vertical error bars represent statistical fluctuations at a 95% confidence interval.

Theory

The full set of electronic PESs is identical for C-H₂ and C-D₂ systems and depends only on the mutual distances of the three atoms involved. Hence, in our scattering calculations of C(³P_{*j*}) with *o*- and *p*-D₂ we employed the most recent highly-correlated C(³P_{*j*})-H₂ PESs of Kłos et al. (2018) that were computed with the explicitly correlated multireference configuration interaction method (ic-MRCI-F12) (Shiozaki and Werner, 2011, 2013; Shiozaki et al., 2011) with large atomic basis set. Briefly, the interaction of the open-shell C(³P_{*j*}) atom with the H₂ molecule gives rise to two adiabatic potentials of the A'' symmetry (wave function anti-symmetric with respect to the reflection in three-atomic plane) and one of A' symmetry (symmetric with respect to the in-plane reflection). The two adiabatic potentials were diabaticized before the dynamical calculations and the diabaticization procedure provided additional off-diagonal coupling. We refer the readers to Kłos et al. (2018) for more details about *ab initio* calculations of the PESs. The geometry of the H₂ molecule in the C-H₂ PESs is fixed at the $r_0 = 0.767$ Å distance corresponding to an average over the lowest vibrational state $v = 0$ and considered as a rigid rotor. As we substitute both H atoms with D isotopologs, we do not need to modify center of mass of the diatomic as the molecule is still homonuclear. In a case of a single isotope substitution to form an HD molecule, one would need to shift the center of mass accordingly. The rigid rotor approach for C-H₂ and C-D₂ can use the same set of rigid rotor 2-dimensional PESs assuming that we neglect any mass effects in description of H₂ and D₂ that can change slightly the equilibrium distance. The difference between vibrationally averaged distance r_0 for the D₂ molecule and H₂ molecule

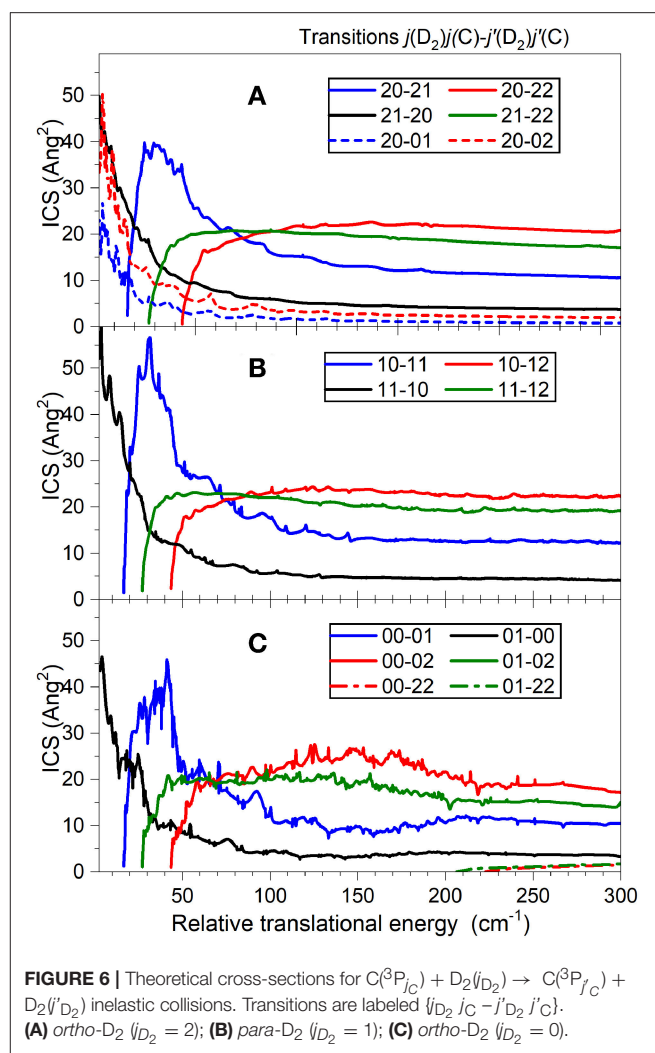


FIGURE 6 | Theoretical cross-sections for C(³P_{*j*}) + D₂(*v*D₂) → C(³P_{*j'*}) + D₂(*v'*D₂) inelastic collisions. Transitions are labeled $j_{D_2} j_C - j'_{D_2} j'_C$. (A) *ortho*-D₂ ($v_{D_2} = 2$); (B) *para*-D₂ ($v_{D_2} = 1$); (C) *ortho*-D₂ ($v_{D_2} = 0$).

is only about 0.008 Å. Therefore, within these assumptions and approximations we can use our C-H₂ PESs for the C-D₂ system.

To obtain integral cross-sections we solved Close-Coupling equations of Arthurs and Dalgarno (1960) using the HIBRIDON package¹. For the C(³P_{*j*})-D₂ scattering we use the reduced mass of 3.0158368 a.m.u. The rotational constant of the D₂ molecule (Huber and Herzberg, 1979) is $B_0 = 29.9037$ cm⁻¹ and the spin-orbit energy levels of C(³P_{*j*}) atom (Cooksy et al., 1986; Yamamoto and Saito, 1991), listed in NIST basic atomic spectroscopic data are 0, 16.42 and 43.41 cm⁻¹ for C(³P₀), C(³P₁), and C(³P₂), respectively. The Close-Coupling equations are propagated using hybrid Alexander-Manolopoulos propagator from the initial distance of $R = 1.0$ to 80 a_0 . The cross-sections were checked for

¹Hibridon is a Package of Programs for the Time-Independent Quantum Treatment of Inelastic Collisions and Photodissociation written by M. H. Alexander, D. E. Manolopoulos, H.-J. Werner, and B. Follmeg, with contributions by P. F. Vohralik, D. Lemoine, G. Corey, R. Gordon, B. Johnson, T. Orlikowski, A. Berning, A. Degli-Esposti, C. Rist, P. J. Dagdigian, B. Pouilly, G. van der Sanden, M. Yang, F. de Weerd, S. Gregurick, J. Kłos and F. Lique. Available online at: <http://www2.chem.umd.edu/groups/alexander/hibridon/hib43/>

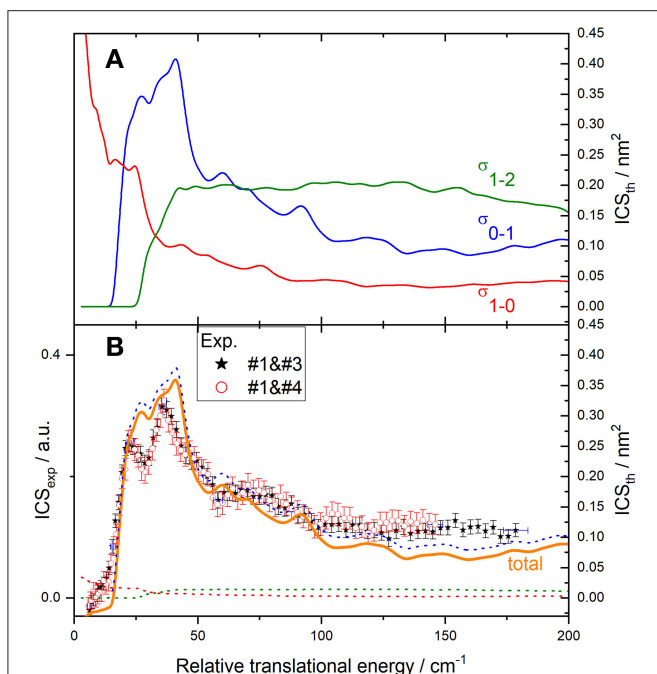


FIGURE 7 | Experimental and theoretical cross-sections for $C(^3P_0) + o\text{-}D_2 \rightarrow C(^3P_1) + o\text{-}D_2$ inelastic collisions. **(A)** theory convoluted to experimental resolution for individual transitions of $C(^3P_j)$ with $o\text{-}D_2(j_{D_2} = 0)$: $C(^3P_0) \rightarrow C(^3P_1)$ (blue solid line), $C(^3P_0) \rightarrow C(^3P_2)$ (green solid line), and $C(^3P_1) \rightarrow C(^3P_0)$ (red solid line); **(B)** experiment (red open circles in the conditions #1 and #4 and black stars in the conditions #1 and #3 described in **Table 1**); theoretical contributions of transitions $C(^3P_0) \rightarrow C(^3P_1)$ (blue dotted line), $C(^3P_1) \rightarrow C(^3P_2)$ (green dotted line), $C(^3P_1) \rightarrow C(^3P_0)$ (red dotted line), and total (orange solid line), assuming a 7% initial population of $C(^3P_1)$; $C(^3P_2)$ is populated by $C(^3P_0) \rightarrow C(^3P_1)$ (main contribution) and depopulated by $C(^3P_1) \rightarrow C(^3P_2)$ and $C(^3P_1) \rightarrow C(^3P_0)$ transitions, resulting in a total $ICS_{tot} = 0.93 \sigma_{0-1} - 0.07 (\sigma_{1-2} + \sigma_{1-0})$. To allow for easier comparison, experimental ICS scale is adjusted such that the area in the $[22 - 116] \text{ cm}^{-1}$ range is the same as for the theoretical ICS calculated. Vertical error bars represent the statistical uncertainties at the 95% confidence interval; each point corresponds to 2020 (experimental conditions #1 and #4) and 1680 (experimental conditions #1 and #3) laser shots per angle, scanning the beam intersection angle between 90° and 13° , with -1° decrement. The plotted error bars on energy are estimated from velocity and crossing angle uncertainties.

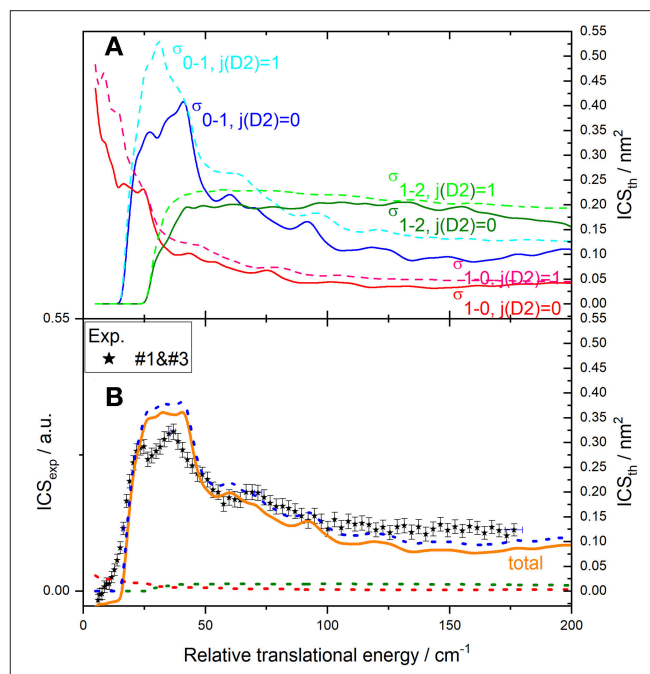


FIGURE 8 | Experimental and theoretical cross-sections for $C(^3P_0) + n\text{-}D_2 \rightarrow C(^3P_1) + n\text{-}D_2$ inelastic collisions. **(A)** theory convoluted to experimental resolution for individual transitions of $C(^3P_j)$ with $D_2(j_{D_2} = 0)$ and $D_2(j_{D_2} = 1)$: $C(^3P_0) \rightarrow C(^3P_1)$ (blue solid line and cyan dashed line), $C(^3P_1) \rightarrow C(^3P_2)$ (green solid line and dashed line), $C(^3P_1) \rightarrow C(^3P_0)$ (red solid line and pink dashed line); **(B)** experiment (black stars in the conditions #1 and #3 described in **Table 1**); theoretical contributions of transitions $C(^3P_0) \rightarrow C(^3P_1)$ (blue dotted line), $C(^3P_1) \rightarrow C(^3P_2)$ (green dotted line), $C(^3P_1) \rightarrow C(^3P_0)$ (red dotted line), and total (orange solid line), assuming that $n\text{-}D_2$ is composed of 33% of $j_{D_2} = 1$ and 66% of $j_{D_2} = 0$ and a 7% initial population of $C(^3P_1)$; $C(^3P_1)$ is populated by $C(^3P_0) \rightarrow C(^3P_1)$ (main contribution) and depopulated by the $C(^3P_1) \rightarrow C(^3P_2)$ and $C(^3P_1) \rightarrow C(^3P_0)$ transitions by collision with $D_2(j_{D_2} = 0)$ and $D_2(j_{D_2} = 1)$, resulting in a total $ICS_{tot} = 0.93 (0.33\sigma_{0-1,j(D_2)=1} + 0.66\sigma_{0-1,j(D_2)=0}) - 0.07 \{0.33(\sigma_{1-2,j(D_2)=1} + \sigma_{1-0,j(D_2)=1}) + 0.66(\sigma_{1-2,j(D_2)=0} + \sigma_{1-0,j(D_2)=0})\}$. To allow for easier comparison, experimental ICS scale is adjusted such that the area in the $[22 - 114] \text{ cm}^{-1}$ range is the same as for the theoretical ICS calculated. Vertical error bars represent the statistical uncertainties at the 95% confidence interval; each point corresponds to 2060 laser shots per angle, scanning the beam intersection angle between 90° and 14° , with -1° decrement. The plotted error bars on energy are estimated from velocity and crossing angle uncertainties.

convergence with respect to the inclusion of a sufficient number of partial waves and energetically closed channels. The $o\text{-}D_2$ basis included all levels with a rotational quantum number $j_{D_2} \leq 6$. State-to-state excitation cross-sections were obtained between all the fine-structure levels of $C(^3P)$ over the collision energy range relevant to the experiments ($0 - 800 \text{ cm}^{-1}$) on the grid of energies with a step of 0.1 cm^{-1} (see **Figure 6**). $C\text{-}H_2$ and $C\text{-}D_2$ calculations differ by the different energy structure of the partners and by a different reduced mass.

RESULTS AND DISCUSSION

As expected, the excitation functions, i.e., the variation of the ICSs as a function of relative translation energy, for $C(^3P_0) + D_2 \rightarrow C(^3P_1) + D_2$ and $C(^3P_0) + D_2 \rightarrow$

$C(^3P_2) + D_2$ (**Figures 7–11**) all exhibit a threshold behavior corresponding to the spin-orbit energy differences: $E(^3P_1) - E(^3P_0) = 16.42 \text{ cm}^{-1}$ and $E(^3P_2) - E(^3P_0) = 43.41 \text{ cm}^{-1}$. In **Figure 6** are displayed the calculated ICSs for all transitions which may contribute to the observed signals. It is worth noting that the ICSs for relaxation transitions rapidly decrease at high energies. To allow for comparison with experimental data, these ICSs were convoluted with the experimental energy resolution (**Figure 12**).

$C(^3P_0) + o(n)\text{-}D_2 \rightarrow C(^3P_1) + o(n)\text{-}D_2$ Transitions

Results for the $C(^3P_0)$ excitation by collision with $o\text{-}$ and $n\text{-}D_2$ are displayed in **Figures 7, 8**, respectively. The convoluted theoretical

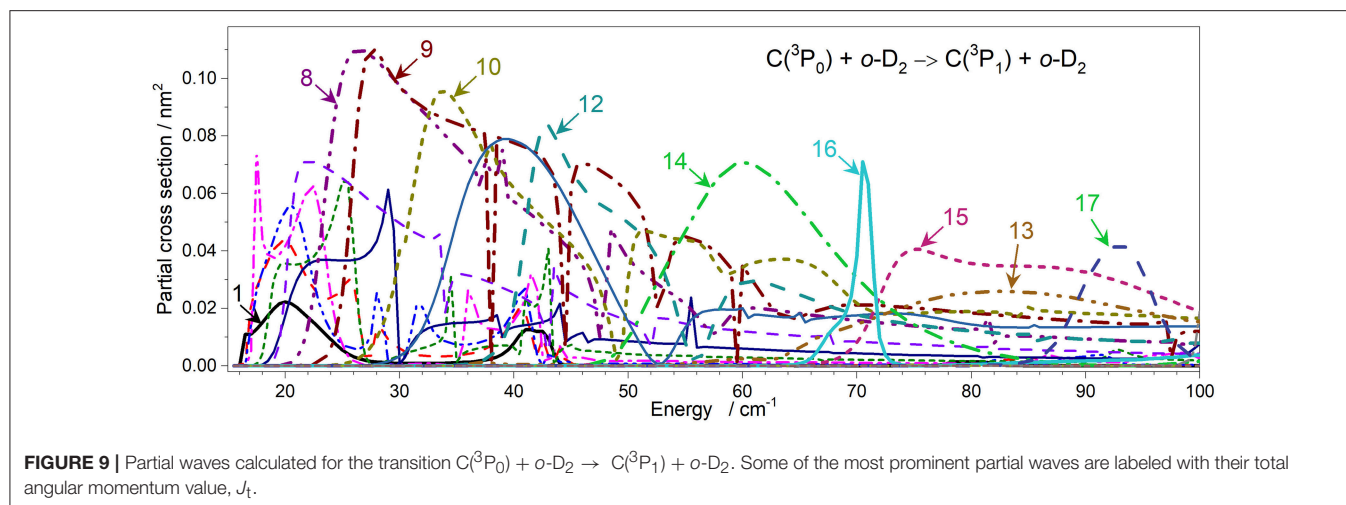


FIGURE 9 | Partial waves calculated for the transition $C(^3P_0) + o\text{-D}_2 \rightarrow C(^3P_1) + o\text{-D}_2$. Some of the most prominent partial waves are labeled with their total angular momentum value, J_t .

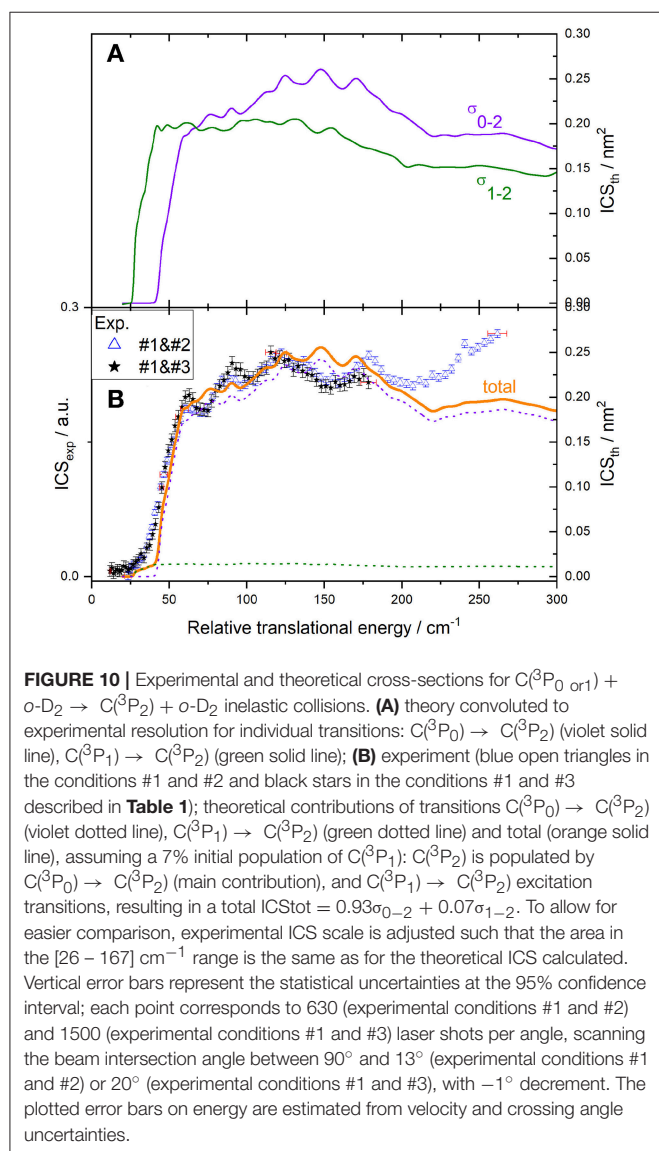
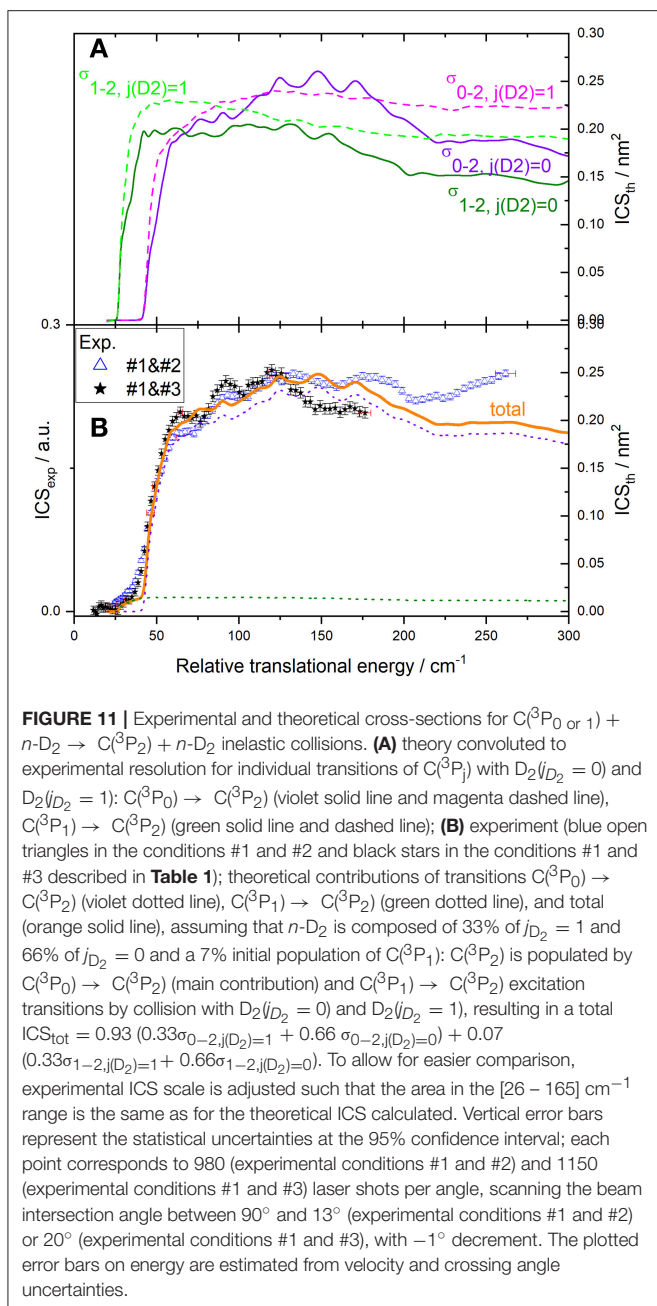


FIGURE 10 | Experimental and theoretical cross-sections for $C(^3P_0 \text{ or } 1) + o\text{-D}_2 \rightarrow C(^3P_2) + o\text{-D}_2$ inelastic collisions. **(A)** theory convoluted to experimental resolution for individual transitions: $C(^3P_0) \rightarrow C(^3P_2)$ (violet solid line), $C(^3P_1) \rightarrow C(^3P_2)$ (green solid line); **(B)** experiment (blue open triangles in the conditions #1 and #2 and black stars in the conditions #1 and #3 described in **Table 1**); theoretical contributions of transitions $C(^3P_0) \rightarrow C(^3P_2)$ (violet dotted line), $C(^3P_1) \rightarrow C(^3P_2)$ (green dotted line) and total (orange solid line), assuming a 7% initial population of $C(^3P_1)$: $C(^3P_2)$ is populated by $C(^3P_0) \rightarrow C(^3P_2)$ (main contribution), and $C(^3P_1) \rightarrow C(^3P_2)$ excitation transitions, resulting in a total $ICS_{\text{tot}} = 0.93\sigma_{0-2} + 0.07\sigma_{1-2}$. To allow for easier comparison, experimental ICS scale is adjusted such that the area in the [26 – 167] cm^{-1} range is the same as for the theoretical ICS calculated. Vertical error bars represent the statistical uncertainties at the 95% confidence interval; each point corresponds to 630 (experimental conditions #1 and #2) and 1500 (experimental conditions #1 and #3) laser shots per angle, scanning the beam intersection angle between 90° and 13° (experimental conditions #1 and #2) or 20° (experimental conditions #1 and #3), with -1° decrement. The plotted error bars on energy are estimated from velocity and crossing angle uncertainties.

ICSs for involved transitions, given in the upper panels, are also displayed in the lower panels weighted by their estimated contributions to the total process: due to the presence of a small amount of $C(^3P_1)$, transitions $C(^3P_1) \rightarrow C(^3P_0)$ and $C(^3P_1) \rightarrow C(^3P_2)$ need to be taken into account. The resulting total ICS can then be compared to experimental results.

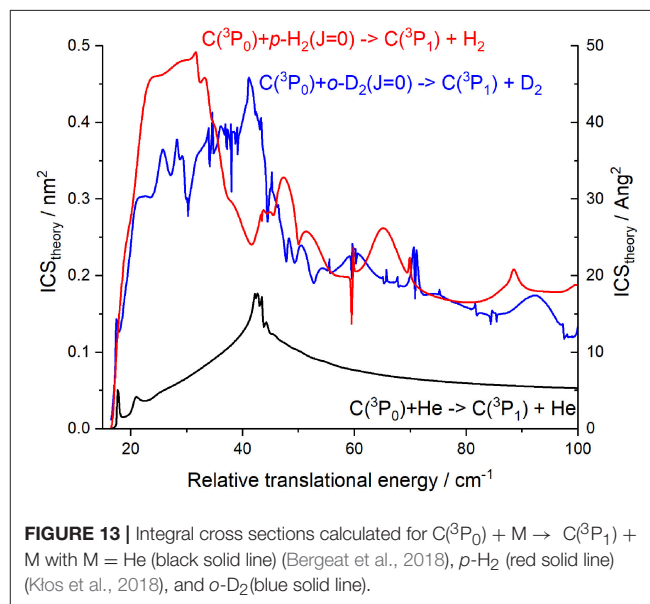
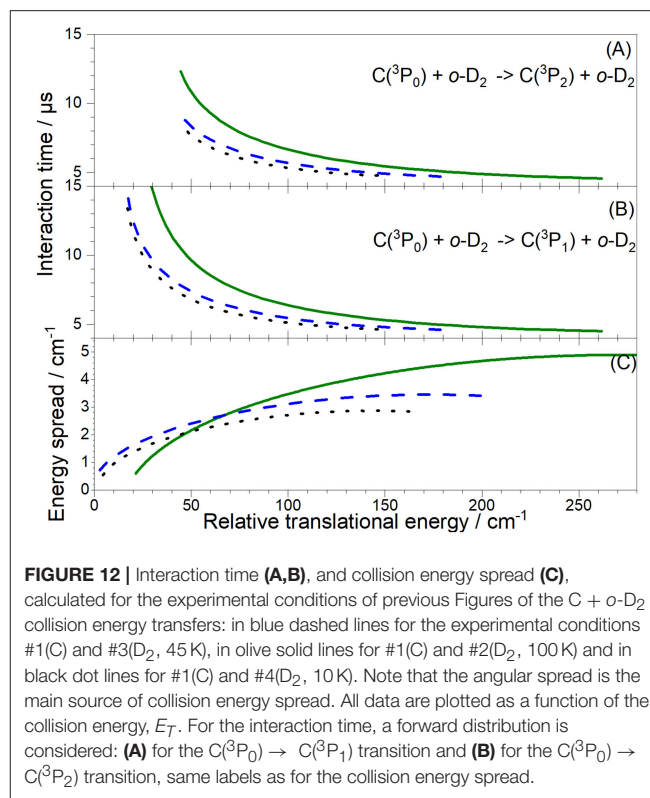
For collisions with $o\text{-D}_2$ (**Figure 7**), two sets of experiments were achieved, under different D_2 -beam conditions, with different velocities: consequently, data for a given energy have been acquired at different crossing angles. The excellent agreement between both experimental sets ensures the absence of any bias in the method used to recover the ICS from the REMPI signal, which involves estimating the mean interaction time $\langle \Delta t \rangle$, which depends on the crossing angle (**Figure 12**). Only transitions involving D_2 ($j_{D_2} = 0$) are taken into account in the overall convoluted theoretical ICS, which indeed is not the case for collisions with $n\text{-D}_2$ (**Figure 8**), where transitions involving D_2 ($j_{D_2} = 1$) also need to be taken into account with relative weights of 2/3 and 1/3, respectively.

Resonance structures observed experimentally are very similar to the theoretical ones, however slightly shifted in energy. The agreement is better for $o\text{-D}_2$ than for $n\text{-D}_2$, since more contributions are involved in the latter case. In particular, the first two peaks at *ca.* 26.5 and 41.3 cm^{-1} for $j_{D_2} = 0$ are well resolved in both theory and experiment for $o\text{-D}_2$ (**Figure 7A**), but are blurred out by the peak at *ca.* 31 cm^{-1} for $j_{D_2} = 1$ for $n\text{-D}_2$ (**Figure 8B**). In **Figure 9** are displayed partial cross sections for $C(^3P_0) \rightarrow C(^3P_1)$ corresponding to partial waves with total angular momenta J_t from 1 to 20 that contribute within the 16–100 cm^{-1} total energy range. The peaks around 20 and 40 already appear at $J_t = 1$ (thick black solid line) and are associated with opening of carbon spin orbit channels. The first lowest partial waves form sharp peaks around 20 cm^{-1} , whereas a broader peak around $30\text{--}40 \text{ cm}^{-1}$ is due to the build-up of partial waves with $J_t = 8\text{--}12$. The peak around 60 cm^{-1} comes from a shape resonance for $J_t = 14$. A sharp shape resonance also appears for $J_t = 17$ near 90 cm^{-1} .



C(³P₀) + o(n)-D₂ → C(³P₂) + o(n)-D₂ Transitions

Results for the $C(^3P_0)$ excitation by collision with o - and n -D₂ are displayed in **Figures 10, 11**. The convoluted theoretical ICSs for involved transitions, given in the upper panels, are also displayed in the lower panels weighted by their estimated contributions to the total process: again, due to the presence of a small amount of $C(^3P_1)$, transition $C(^3P_1) \rightarrow C(^3P_2)$ need to be taken into account. Note that the collisional de-excitation of $C(^3P_2)$ is not taken into account here since its initial population is negligible: furthermore, it would result in a negative offset below threshold



not observed. The resulting total ICS can then be compared to experimental results.

In both cases, two sets of experiments were achieved, under different D₂-beam conditions, with different velocities. Whereas both experimental sets are in good agreement for $o\text{-D}_2$ (**Figure 10B**) up to 160 cm^{-1} , it is not the case for $n\text{-D}_2$ experiments. However, the beam velocity mismatch is larger for

C(³P₀) → C(³P₂) experiments ($v_c = 815$; $v_{D_2} = 845$ and 1180 ms⁻¹, resulting in $E_T = 179$ and 262 cm⁻¹ at $\chi = 90^\circ$) than for C(³P₀) → C(³P₁) experiments ($v_c = 815$; $v_{D_2} = 694$ and 855 ms⁻¹, resulting in $E_T = 146$ and 179 cm⁻¹ at $\chi = 90^\circ$): at 90° , the interaction time is much shorter than at lower angles: a variation (even small) in its estimated value can result in a larger variation of the ICS value ($= I_{\text{REMPI}}/(v_r \langle \Delta t \rangle)$). It is however worth noting that the increase of the cross-section at high energies is too high to be due to a $\langle \Delta t \rangle$ possible underestimate. It could be due to an energy transfer involving relaxation of D₂ ($j_{D_2} = 2 \rightarrow 0$): however, ICSs involving such a relaxation are monotonously decreasing (Figure 6), which would imply that their contribution should be much more intense at low energies resulting in a significant positive offset not observed. Furthermore, ICSs corresponding to rotational (de-)excitation of D₂ are weak (Figure 6). This is due to a weak anisotropy of the PES with respect to D₂ rotation that leads to a weak coupling between the D₂ rotational states. It also explains that the magnitudes of the ICSs are similar for all D₂ rotational state. In addition, the energy splitting between $j_{D_2} = 0$ and $j_{D_2} = 2$ state of D₂ is so large that the excitation probability is very small.

Another possibility to be considered is the coupling with the C(¹D₂) state: its crossing with triplet PESs is estimated around 300 cm⁻¹ by theory. Excitation to the ¹D₂ state is closed but the increase of the ICS may be due to indirect coupling that will favor the ³P₂ state over the ³P₁. This would result in a decrease of the ICS for the ³P₁ in the same energy domain (not probed in the present experiments).

The cross-sections observed are different in shape, but almost similar in average. Resonances are less visible for the C(³P₀) → C(³P₂) than for C(³P₀) → C(³P₁) ICS: actually, there are many more resonances for the 0–2 transition than for 0–1, especially for $j_{D_2} = 1$, resulting in a smoother shape. On average, their amplitudes differ by a factor of ~ 2 . Similar differences were found for the O–H system (Lique et al., 2018). The fact that the C(³P₀) – C(³P₂), C(³P₁) – C(³P₂), and C(³P₀) – C(³P₁) transitions have more or less the same magnitude may be partly explained by the huge well depth that would lead to a significant redistribution of the flux over all open C-atom spin-orbit states.

Comparison of C–D₂ With C–H₂ and C–He Systems

As shown in Figure 13, there is a great difference between C–He and C–H₂ (D₂) systems, due to quite different excitation processes. For C–He, the interaction is a weak van der Waals forces and the excitation is thus essentially governed by spin-orbit coupling (Bergeat et al., 2018). For C–H₂ (D₂), the interaction consists in a deep potential well and the system can then be chemically bound and collisional energy transfers therefore are much more efficient, as clearly shown in Figure 13. However, there is a decrease in the C(³P₀) – C(³P₁) ICSs around 50 cm⁻¹

for all systems, essentially due to the opening of the C(³P₀) – C(³P₂) excitation. Concerning C–D₂ and C–H₂ systems, apart the resonances, ICSs are expected to be similar when no rotational (de-)excitation of H₂ (D₂) is involved as can be seen in Figure 13.

CONCLUSION

In this work, we have presented a joint theoretical and experimental study of the spin-orbit transitions of C(³P_j) by collisions with D₂. Integral cross-sections have been experimentally observed in a crossed beam apparatus down to collision energies below *ca.* 5.5 cm⁻¹ (66 J mol⁻¹) and compared to state-of-the-art non-Born-Oppenheimer quantum dynamical calculations for C(³P₀) → C(³P₁) and C(³P₀) → C(³P₂) transitions. Results have been compared to similar systems previously studied (C(³P_j) + H₂, and He) (Bergeat et al., 2018; Kłos et al., 2018). The overall agreement obtained, in particular for C(³P_j) + H₂ and C(³P_j) + D₂ for which calculations are performed using the same potential energy surfaces, confirms the validity of these potentials which can be confidently used to compute (de-)excitation rates of C-atoms in the low energy domain relevant to astrophysical modeling of cold molecular clouds. However, the present results validate the low energy data generated from these PESs but the calculations at higher energy would require to revise the theoretical approach and probably to add the excited state of C-atom.

DATA AVAILABILITY

All datasets generated for this study are included in the manuscript and are available on request.

AUTHOR CONTRIBUTIONS

AB, SM, and CN carried out the experimental measurements and data analysis. FL and JK performed the theoretical calculations. The manuscript was written through contributions of all authors.

FUNDING

This work was supported by the Programme National Physique et Chimie du Milieu Interstellaire (PCMI) of CNRS/INSU with INC/INP co-funded by CEA and CNES. AB, FL, SM, and CN acknowledge also financial support from the Agence Nationale de la Recherche, contract Hydrides (ANR-12-B505-0011-02). JK acknowledges financial support from the U. S. National Science Foundation, under the grant No. CHE-1565872 to M. H. Alexander.

REFERENCES

- Arthurs, A. M., and Dalgarno, A. (1960). The theory of scattering by a rigid rotator. *Proc. R. Soc. Lond. Ser. A* 256:540. doi: 10.1098/rspa.1960.0125
- Bensby, T., and Feltzing, S. (2006). The origin and chemical evolution of carbon in the Galactic thin and thick discs. *Mon. Not. R. Astron. Soc.* 367, 1181–1193. doi: 10.1111/j.1365-2966.2006.10037.x

- Bergeat, A., Chefdeville, S., Costes, M., Morales, S. B., Naulin, C., Even, U., et al. (2018). Understanding the quantum nature of low-energy C(³P_j) + He inelastic collisions. *Nat. Chem.* 10, 519–522. doi: 10.1038/s41557-018-0030-y
- Born, M., and Oppenheimer, R. (1927). Zur Quantentheorie der Molekeln. *Ann. Phys.* 389, 457–484. doi: 10.1002/andp.19273892002
- Chefdeville, S., Kalugina, Y., van de Meerakker, S. Y. T., Naulin, C., Lique, F., and Costes, M. (2013). Observation of partial wave resonances in low-energy O₂-H₂ inelastic collisions. *Science* 341, 1094–1096. doi: 10.1126/science.1241395
- Chefdeville, S., Stoecklin, T., Bergeat, A., Hickson, K. M., Naulin, C., and Costes, M. (2012). Appearance of low energy resonances in CO-Para-H₂ inelastic collisions. *Phys. Rev. Lett.* 109:023201. doi: 10.1103/PhysRevLett.109.023201
- Cooksy, A. L., Saykally, R. J., Brown, J. M., and Evenson, K. M. (1986). Accurate determination of the fine-structure intervals in the 3P ground states of ¹³C and ¹²C by far-infrared laser magnetic resonance. *Astrophys. J.* 309, 828–832. doi: 10.1086/164651
- Even, U. (2015). The Even-Lavie valve as a source for high intensity supersonic beam. *EPJ Tech. Instrum.* 2:17. doi: 10.1140/epjti/s40485-015-0027-5
- Geppert, W. D., Naulin, C., Costes, M., Capozza, G., Cartechini, L., Casavecchia, P., et al. (2003). Combined crossed-beam studies of C(³P_j) + C₂H₄ → C₃H₃ + H reaction dynamics between 0.49 and 30.8 kJ mol⁻¹. *J. Chem. Phys.* 119, 10607–10617. doi: 10.1063/1.1619374
- Herbst, E., and Yates, J. T. Jr. (2013). Introduction: astrochemistry. *Chem. Rev.* 113, 8707–8709. doi: 10.1021/cr400579y
- Huber, K. P., and Herzberg, G. (1979). “Molecular spectra and molecular structure,” in *Constants of Diatomic Molecules*, Vol. 4 (New York, NY: Van Nostrand Reinhold), 262–267. doi: 10.1007/978-1-4757-0961-2
- Kłos, J., Bergeat, A., Vanuzzo, G., Morales, S. B., Naulin, C., and Lique, F. (2018). Probing nonadiabatic effects in low-energy C(³P_j) + H₂ collisions. *J. Phys. Chem. Lett.* 9, 6496–6501. doi: 10.1021/acs.jpcllett.8b03025
- Lique, F., Kłos, J., Alexander, M. H., Le Picard, S. D., and Dagdigan, P. J. (2018). Fine-structure relaxation of O(³P) induced by collisions with He, H and H₂. *MNRAS* 474, 2313–2322. doi: 10.1093/mnras/stx2907
- Naulin, C., and Bergeat, A. (2018). “Low energy scattering in crossed molecular beams,” in *Cold Chemistry: Molecular Scattering and Reactivity Near Absolute Zero*, eds O. Dulieu and A. Osterwalder (Royal Society of Chemistry), 92–149. doi: 10.1039/9781782626800-00092
- Naulin, C., and Costes, M. (2014). Experimental search for scattering resonances in near cold molecular collisions. *Int. Rev. Phys. Chem.* 33, 427–446. doi: 10.1080/0144235X.2014.957565
- Pentlehner, D., Riechers, R., Dick, B., Slenczka, A., Even, U., Lavie, N., et al. (2009). Rapidly pulsed helium droplet source. *Rev. Sci. Instrum.* 80:043302. doi: 10.1063/1.3117196
- Shen, Z., Ma, H., Zhang, C., Fu, M., Wu, Y., Bian, W., et al. (2017). Dynamical importance of van der Waals saddle and excited potential surface in C(¹D) + D₂ complex-forming reaction. *Nat. Commun.* 8:14094. doi: 10.1038/ncomms14094
- Shiozaki, T., Knizia, G., and Werner, H.-J. (2011). Explicitly correlated multireference configuration interaction: MRCI-F12. *J. Chem. Phys.* 134:034113. doi: 10.1063/1.3528720
- Shiozaki, T., and Werner, H.-J. (2011). Explicitly correlated multireference configuration interaction with multiple reference functions: avoided crossings and conical intersections. *J. Chem. Phys.* 134:184104. doi: 10.1063/1.3587632
- Shiozaki, T., and Werner, H.-J. (2013). Multireference explicitly correlated F12 theories. *Mol. Phys.* 111:607. doi: 10.1080/00268976.2013.779393
- Yamamoto, S., and Saito, S. (1991). Laboratory observation of the ³P₁-³P₀ transition of the neutral carbon atom by submillimeter-wave absorption spectroscopy. *Astrophys. J.* 370, L103–L105. doi: 10.1086/185987
- Zmuidzinas, J., Betz, A. L., Boreiko, R. T., and Goldhaber, D. M. (1988). Neutral atomic carbon in dense molecular clouds. *Astrophys. J.* 335, 774–785. doi: 10.1086/166966

Conflict of Interest Statement: The authors declare that the research was conducted in the absence of any commercial or financial relationships that could be construed as a potential conflict of interest.

Copyright © 2019 Bergeat, Morales, Naulin, Kłos and Lique. This is an open-access article distributed under the terms of the Creative Commons Attribution License (CC BY). The use, distribution or reproduction in other forums is permitted, provided the original author(s) and the copyright owner(s) are credited and that the original publication in this journal is cited, in accordance with accepted academic practice. No use, distribution or reproduction is permitted which does not comply with these terms.